

Matterhorn: Efficient Analog Sparse Spiking Transformer Architecture with Masked Time-To-First-Spike Encoding

Zhanglu Yan¹ Kaiwen Tang¹ Zixuan Zhu^{1,2,3} Zhenyu Bai¹ Qianhui Liu⁴ Weng-Fai Wong¹

Abstract

Spiking neural networks (SNNs) have emerged as a promising candidate for energy-efficient LLM inference. However, current energy evaluations for SNNs primarily focus on counting accumulate operations, and fail to account for real-world hardware costs such as data movement, which can consume nearly 80% of the total energy. In this paper, we propose Matterhorn, a spiking transformer that integrates a novel masked time-to-first-spike (M-TTFS) encoding method to reduce spike movement and a memristive synapse unit (MSU) to eliminate weight access overhead. M-TTFS employs a masking strategy that reassigns the zero-energy silent state (a spike train of all 0s) to the most frequent membrane potential rather than the lowest. This aligns the coding scheme with the data distribution, minimizing spike movement energy without information loss. We further propose a ‘dead zone’ strategy that maximizes sparsity by mapping all values within a given range to the silent state. At the hardware level, the MSU utilizes compute-in-memory (CIM) technology to perform analog integration directly within memory, effectively removing weight access costs. On the GLUE benchmark, Matterhorn establishes a new state-of-the-art, surpassing existing SNNs by 1.42% in average accuracy while delivering a 2.31 \times improvement in energy efficiency.

1. Introduction

Spiking neural networks (SNNs) have emerged as energy-efficient alternatives to traditional artificial neural networks (ANNs), gaining renewed popularity as researchers increas-

¹Department of computer science, National University of Singapore ²Shanghai Advanced Research Institute, Chinese Academy of Science ³ University of Chinese Academy of Sciences, Beijing ⁴School of Artificial Intelligence, Shandong University. {zlyan,zhenyu.bai,wongwf}@nus.edu.sg, zhuzixuan@sari.ac.cn, qhliu@sdu.edu.cn .

ingly apply spiking architectures to build energy-efficient large language models (LLMs) (Wang et al., 2025; Xing et al., 2024a). However, current evaluations often rely on simplified metrics that fail to account for real-world hardware costs. Existing studies largely attribute energy savings of SNNs to the replacement of multiply-and-accumulate (MAC) operations with cheaper accumulate (ACC) operations. For instance, Sorbet (Tang et al., 2025) and SpikingLM (Xing et al., 2024b) report 27.16 \times and 12.9 \times efficiency gains, respectively, based solely on operation counts. Such metrics always overlook other, perhaps even more, significant overhead of hardware implementation (Yan et al., 2024; Dampfhofer et al., 2023). As shown in Figure 1, our measurements of SOTA spiking transformers on a commercial 22nm process show that the ACC computing energy (membrane potential accumulation and spiking process) accounts for only 12–20% of the total energy. In contrast, data movement dominates the energy profile: spike transfers (inter-core communication) represent 42–55%, while weight access (SRAM reads) accounts for 27–32%. Consequently, the energy of this data movement is essential for achieving a truly efficient SNN.

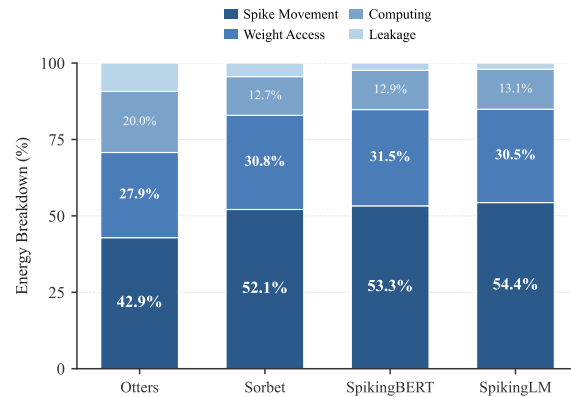


Figure 1. Proportional Energy Breakdown of SOTA spiking transformers. Otters (standard TTFS encoding version is chose), Sorbet (rate encoding), SpikingBERT (rate encoding), and SpikingLM (rate encoding) are evaluated with time steps T set to 15, 16, 16, and 4, and average spike rates of 5.14%, 13%, 25%, and 33%, respectively, as reported in (Bal & Sengupta, 2024; Xing et al., 2024b; Tang et al., 2025; Yan et al., 2025a). SNN models are assumed to be deployed on a spatial dataflow architecture as described in Section 2.3.

Unlike ANNs which compress information into high-density n -bit integers, SNNs temporally expand data into sparse binary *spike trains* with a fixed size *time window* of T (Yan et al., 2025b). Such temporal expansion has the unique potential for energy-efficient inter-core activation communication. Specifically, while ANNs must transfer multi-bit integers in a single pass, SNNs transmit only single-bit binary spikes because of their event-based nature. To realize these energy advantages, a low spike rate is essential to ensure that the energy benefits of single-bit communication outweigh the temporal overhead of T time steps. Common encoding methods for spiking transformers primarily rely on *rate* or *time-to-first-spike* (TTFS) encoding. While rate encoding is commonly used, it suffers from a relatively high spike rate (10-30%) (Bal & Sengupta, 2024; Xing et al., 2024b; Tang et al., 2025). In contrast, TTFS achieves superior efficiency by enforcing an “at most one spike” constraint, reducing activity to $\sim 5\%$ (Yan et al., 2025a).

Despite its low spike rate, TTFS has other structural inefficiency. Traditionally, this encoding follows a fixed rule where higher membrane potentials result in earlier spike times. This assigns the zero-energy silent state (the all-zero spike train) only to the smallest possible value. However, as such a value is a rare outlier in spiking transformers (Wang et al., 2025; Xiao et al., 2023), the conventional mapping wastes the energy-saving silent state on rare occurrences, while more frequently occurring values result in spikes. This inefficiency raises a fundamental question: *must the encoding be necessarily such that larger values spike first?* We propose otherwise. The core efficacy of TTFS stems from its sparsity constraint of transferring at most one spike rather than its specific temporal sequence. As long as the mapping is deterministic, the spike order can be optimized for hardware efficiency without sacrificing information.

Based on this insight, we propose a new spike encoding method, *masked time-to-first-spike* (M-TTFS). By incorporating a temporal mask to inhibit spikes at the most frequent firing time, denoted as I_{\max} , we reassign the silent state to represent the most common activation values. For instance, if the distribution of accumulated membrane potentials peaks at time step $t = 7$, our method suppresses spike generation at this specific time step, thereby silencing the majority of inputs. Our experiment running M-TTFS on the SST-2 benchmark showed an average reduction from 4.07% to 2.77% in spike rate, lowering the spike movement energy of the attention block from 6.98 mJ to 4.75 mJ with no loss in accuracy. Furthermore, we introduce a ‘dead zone’ strategy governed by a tunable integer range k . To maximize sparsity, this strategy maps all spike times within the range $[I_{\max} - k, I_{\max} + k]$ into the silent state. Unlike rate encoding, where the number of spikes is proportional to magnitude (Yan et al., 2023), every nonzero value in our encoding generates exactly one spike regardless of its orig-

inal magnitude. Consequently, we can maximize sparsity by silencing the most frequent activation region instead of a global distribution shift. This approach reduces energy consumption without disrupting the data distribution outside the dead zone. By applying a dead zone with $k = 1$ and $T = 16$, our spiking transformer reduces the overall spike rate to 1.65% and achieves a $2.46\times$ improvement in inter-core spike movement energy compared with traditional TTFS methods.

Beyond data movement, the dead zone also reduces the frequency of weight accesses and computations. However, expanding the dead zone range might incur an accuracy trade-off. This limitation exists because digital optimizations only target the total number of accesses, while the energy cost for each access remains fixed. To fundamentally eliminate these overheads, we shift from the digital domain to an analog-centric mixed-signal domain. Utilizing compute-in-memory (CIM) technology (Ye et al., 2023), we propose the Memristive Synapse Unit (MSU) that leverages physical properties to execute in-memory synaptic integration. Since weights remain stationary during CIM operations, the energy cost of weight access is effectively eliminated. By executing large-scale parallelized multiply-accumulate operations as a single memory read-out in the analog domain, the CIM technique also reduces the unit energy cost of computation. Crucially, this hardware design synergizes with our algorithmic approach: since zero-input currents effectively shut down active analog processing, the sparsity induced by M-TTFS directly translates into physical power gating. The integration of M-TTFS and the MSU compute unit forms our spiking transformer, Matterhorn. By combining algorithmic sparsity to improve spike movement energy with hardware-level efficiency to optimize memory and computing energy, Matterhorn achieves an average accuracy 1.42% higher than previous leading SNNs on the GLUE benchmark, along with a $2.31\times$ improvement in energy efficiency, establishing a high-accuracy and low-energy state-of-the-art spiking transformer².

2. Preliminary

2.1. Time-To-First-Spike encoding

Unlike *artificial neural networks* (ANNs), which transfer information via high-precision integer or floating-point activations, *spiking neural networks* (SNNs) utilize binary spike trains over a time window T . State-of-the-art spiking transformers typically employ one of two encoding mechanisms: *rate* or *temporal* encoding (Che et al., 2025). *Rate encoding* represents information through the firing frequency (the spike count normalized by T). While it achieves accuracy comparable to ANNs in vision and language tasks, it in-

²Code will be released after accept

herently requires high firing activity, limiting energy efficiency (Yan et al., 2023). In contrast, *temporal encoding* like TTFS improves efficiency by generating fewer spikes (Zhao et al., 2025).

Specifically, *time-to-first-spike* (TTFS) encoding carries information solely in the arrival time of the first and only spike within the window T . The operation of a standard TTFS neuron proceeds in two phases: integration and threshold comparison. First, the neuron decodes temporal information using a kernel decay function $f(t)$ (typically $f(t) = T - t$) (Yan et al., 2025a). It updates its membrane potential $V_j^l(t)$ by accumulating weighted inputs from presynaptic neurons:

$$V_j^l(t) = V_j^l(t-1) + \sum_i w_{ij}^l \cdot s_i^{l-1}(t) \cdot f(t) \quad (1)$$

Second, the neuron compares this potential to a firing threshold $\theta^l(t)$. A spike is generated at the specific time step t where the potential meets or exceeds the threshold.

Thus, the firing time is the first instance t such that $V_j^l(t) \geq \theta^l(t)$. If the accumulated potential never exceeds the threshold, the neuron remains silent (a spike train of all zeros). While this silent state maximizes energy efficiency by eliminating data movement costs, it introduces a trade-off. Standard TTFS often suffers from “over-sparsity,” where neurons that fail to fire cannot effectively learn or propagate information (Wei et al., 2023). To address this, we adopt the Dynamic Firing Threshold (DFT) model (Wei et al., 2023), which enforces a synchronous, layer-by-layer schedule to preserve causal relationships. Furthermore, to avoid the convergence instability of direct training, we employ a QNN-to-SNN conversion framework (Yan et al., 2025a).

2.2. Compute-in-memory Architecture

Compute-in-memory (CIM) is a non-Von Neumann architecture designed to mitigate the memory wall bottleneck by performing computation directly within memory arrays. By maintaining a stationary weight matrix, CIM eliminates the high latency and energy costs associated with data movement (Khan et al., 2024). This approach is particularly effective for vector-matrix multiplication (VMM) in neuromorphic computing, offering high parallelism and energy efficiency (Bae et al., 2024). In a CIM array, computation relies on analog circuit laws to perform synaptic integration in a single readout operation. Recent implementations (Ye et al., 2023; Wen et al., 2024) demonstrate energy consumption in the femto-Joule-per-spike (fJ/spike) range, much more efficient than digital baselines.

This work adopts an analog-centric mixed-signal design based on the n-Transistor-1-Resistor (nT1R) crossbar, a typical implementation of the CIM architecture. We select this topology for its power efficiency and control simplic-

ity (Ye et al., 2023). The nT1R cell emulates biological synaptic weights by modulating input spikes via device conductance. We utilize resistive RAM (RRAM) as the core resistor device in nT1R cell due to its high density, CMOS compatibility, and cost-effectiveness (further details in Appendix A). We refer to this specific integration of the nT1R crossbar with customized mixed-signal periphery circuits as the Memristive Synapse Unit (MSU).

2.3. Energy calculation

The total energy consumption is decomposed into two primary components: Computation and Data Movement. Computation includes membrane potential accumulation, decay operations, and threshold comparisons. Data movement encompasses inter-core spike transfer, SRAM access for weights/thresholds, and KV cache read/write (Yan et al., 2024). Our analysis assumes a spatial dataflow architecture where information (e.g., spike packets) is communicated over a Network-on-Chip (NoC). This design is representative of modern specialized hardware, including neuromorphic chips like Loihi (Davies et al., 2018) and dataflow accelerators such as Samanova (Prabhakar et al., 2022). The energy for the Fully Connected (FC) layer (E_{FC}) and Attention Q/K/V computation (E_{qkv}) is defined as:

$$E_{\text{FC}} = N_o^{\text{fc}} \cdot \left[C_i T \left(s_r \underbrace{(E_{\text{Decay}}^{\text{ACC}} + E_{\text{MAC}} + E_{\text{W}}^{\text{Read}} + E_{\text{move}}^{\text{sparse}})}_{\text{Spike Processing}} \right. \right. \\ \left. \left. + E_{\text{leak}} \right) + T \underbrace{(E_{\text{CMP}} + E_{\text{th}}^{\text{Read}})}_{\text{Thresholding}} + \underbrace{E_{\text{kv}}^{\text{Write}}}_{\text{K/V Write}} \right] \quad (2)$$

$$E_{\text{qkv}} = N_o^{\text{qkv}} \cdot \left[d_k T \left(s_r \underbrace{(E_{\text{Enc}}^{\text{ACC}} + E_{\text{MAC}} + E_{\text{move}}^{\text{sparse}} + E_{\text{KV}}^{\text{Read}})}_{\text{Spike Processing}} \right. \right. \\ \left. \left. + E_{\text{leak}} \right) + T \underbrace{(E_{\text{CMP}} + E_{\text{th}}^{\text{Read}})}_{\text{Thresholding}} \right] \quad (3)$$

where $N_o^{\text{fc}} = B \cdot S \cdot C_o$ and $N_o^{\text{qkv}} = B \cdot h \cdot S^2$ represent the total number of output elements. Here, B denotes the batch size, S is the sequence length, C_i/C_o are the input/output channel dimensions, and d_k is the per-head dimension. The term s_r denotes the input spike ratio, which linearly scales the spike processing energy.

3. Methods

3.1. M-TTFS encoding

In standard TTFS, the zero-energy ‘‘silent’’ state (an all-zero spike train) occurs only when the membrane potential fails to cross the threshold by the final time step. M-TTFS fundamentally alters this mapping by reassigning the silent state to the most frequent firing time. By encoding the most common feature values as all-zero spike trains, M-TTFS aligns the coding scheme with the data distribution, effectively maximizing sparsity.

The operation of the M-TTFS neuron proceeds in two phases. First, consistent with traditional TTFS, the neuron integrates incoming spikes to update its membrane potential $V_j^l(t)$ (Equation 1). Second, it performs a masked threshold check. We first define a candidate spike $\hat{s}_j^l(t)$ based on the standard thresholding and first-spike-only constraints:

$$\hat{s}_j^l(t) = \underbrace{H(V_j^l - \theta^l(t))}_{\text{Threshold Check}} \cdot \prod_{\tau=0}^{t-1} (1 - \hat{s}_j^l(\tau)) \quad (4)$$

where $H(\cdot)$ is the Heaviside step function. The product term ensures that the neuron fires at most once per window.

To enforce sparsity, we incorporate a temporal mask $M^l(t)$, which serves as a binary gate to selectively inhibit spike generation. The final output spike $s_j^l(t)$ is derived by applying this mask to the candidate spike $\hat{s}_j^l(t)$. We configure $M^l(t)$ to target the most frequent firing time, denoted as I_{\max} . By setting the mask to zero during this specific interval, we redefine the all-zero spike trains to represent the most frequent feature values:

$$s_j^l(t) = \hat{s}_j^l(t) \cdot \underbrace{M^l(t)}_{\text{Mask Gate}} \quad (5)$$

$$M^l(t) = \begin{cases} 0, & \text{if } t \in (I_{\max} - 1, I_{\max}] \\ 1, & \text{otherwise} \end{cases} \quad (6)$$

Dead zone strategy. Finally, we generalize the masking logic into a ‘‘dead zone’’ strategy to further enhance energy efficiency. Instead of silencing only the single most frequent time step I_{\max} , as shown in Figure 2, we inhibit spikes across a broader range of frequent values centered around I_{\max} . We define the dead zone interval Ω_{dead} with a radius k :

$$\Omega_{\text{dead}} = \{t \mid I_{\max} - k \leq t \leq I_{\max} + k\} \quad (7)$$

Accordingly, the generalized mask function $M(t)$ is configured as:

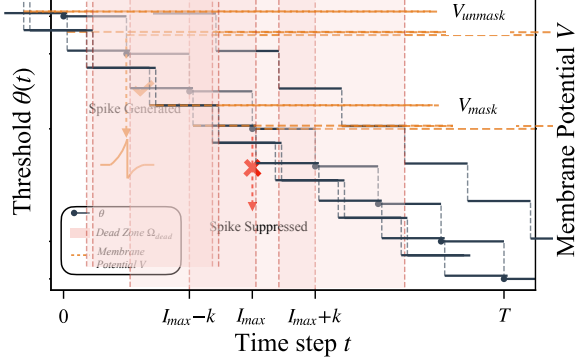


Figure 2. M-TTFS with dead zone.

$$M(t) = \begin{cases} 0, & \text{if } t \in \Omega_{\text{dead}} \\ 1, & \text{otherwise} \end{cases} \quad (8)$$

By adjusting the radius k , we can explicitly control the trade-off between information retention and sparsity.

3.2. QNN-to-SNN conversion

To address the training challenges discussed in Section 2.1, we adopt a QNN-to-SNN conversion framework. This approach involves training a source QNN and mapping its parameters to an M-TTFS SNN to ensure functional equivalence. We first define the QNN layer architecture using symmetric quantization. The quantized output $x_{q,j}^l$ for neuron j is computed as follows:

$$a_j^l = \sum_i w_{ij}^l x_{q,i}^{l-1} + b_j^l \quad (9)$$

$$x_{q,j}^l = \alpha^l \cdot q_j^l = \alpha^l \cdot \text{Clip}(\lfloor \frac{a_j^l}{\alpha^l} \rfloor, -2^{n-1}, 2^{n-1} - 1) \quad (10)$$

where a_j^l denotes the pre-activation, w_{ij}^l and b_j^l are the weights and bias, n represents the quantization bit-width, and α^l is the scaling factor for layer l .

Proposition 1. *An M-TTFS SNN layer incorporating a dead zone Ω_{dead} with radius k is functionally equivalent to a trained n -bit QNN layer (as defined above), provided the following parameter configurations are applied:*

1. *T in SNN matches the QNN resolution, as $T = 2^n$.*
2. *The most frequent QNN activation q_j^l (defined as μ) is aligned with I_{\max} in SNN, and the activation q_j^l within a k -bounded neighborhood is collapsed to μ :*

$$\mu = \frac{T}{2} - 1 - I_{\max}$$

$$q_j^l = \mu \quad \text{if} \quad |q_j^l - \mu| \leq k$$

3. The M-TTFS encoding function $f(t)$ is flattened to μ around I_{\max} :

$$f(t) = \begin{cases} \mu & \text{if } |t - I_{\max}| \leq k \\ \frac{T}{2} - 1 - t & \text{otherwise} \end{cases}$$

4. The firing threshold $\theta^l(t)$ follows the step-wise decreasing function:

$$\theta^l(t) = \alpha^l \cdot \left(\frac{T}{2} - 1 - \lfloor t \rfloor \right)$$

The proof proceeds in two phases. First, we establish that the accumulated membrane potential V_j^l in the SNN is mathematically equivalent to the QNN pre-activation a_j^l during the integration phase. Second, we demonstrate that the QNN masking operation corresponds directly to the SNN dead zone during the firing phase. Together, these steps ensure that the spike firing time t_j^l precisely encodes the quantized output of QNN. A detailed derivation is provided in the Appendix D. We present the full architectural overview of Matterhorn in Figure 3.

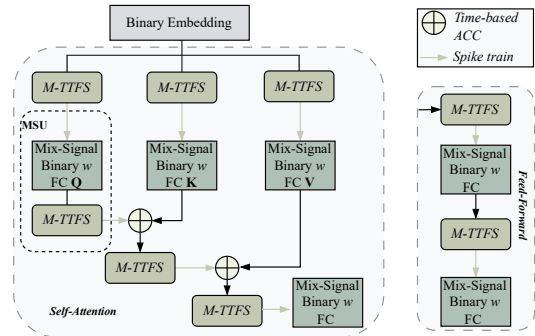


Figure 3. M-TTFS spiking transformer structure.

To satisfy the functional equivalence constraints derived in Proposition 1, we incorporate the dead-zone logic directly into the QNN training loop using knowledge distillation (Liu et al., 2022). In the forward pass, pre-activations are quantized and passed through a dead-zone filter centered at μ . Values falling within a radius k of μ are mapped to μ to simulate the SNN silent state:

$$M_{\text{qnn}} \leftarrow \mathbb{I}(|q_j - \mu| > k) \quad (11)$$

$$q_j^l = (q_j^l \odot M_{\text{qnn}}) + (\mu \odot (1 - M_{\text{qnn}})) \quad (12)$$

During backward propagation, we employ a *masked straight-through estimator* (STE). This mechanism blocks gradients

for values inside the dead zone, ensuring that the network optimizes only for informative features that survive the sparsity constraint. The gradient w.r.t the pre-activation a_j^l is approximated as:

$$\frac{\partial \mathcal{L}}{\partial x_{q,j}^l} \approx \frac{\partial \mathcal{L}}{\partial a_j^l} \cdot \mathbb{I}(-2^{n-1} \leq \frac{x}{\alpha} \leq 2^{n-1} - 1) \odot M_{\text{qnn}} \quad (13)$$

3.3. Memristive synapse unit

We design the *memristive synapse unit* (MSU) to perform synaptic integration by combining a physical analog crossbar (Ye et al., 2023) with digital accumulators. The MSU processes M-TTFS encoded spikes to execute Vector-Matrix Multiplication (VMM). The operation proceeds in three stages: First, input M-TTFS spikes (length T) are decoded into log T -bit integers to maximize the throughput of the analog macro. Second, the MSU performs bit-serial VMM. The log T -bit input vector is fed into the analog crossbar bit-by-bit. For each bit, the crossbar executes a VMM, and the digital accumulators shift and add the partial results. This mixed-signal processing reconstructs the integer VMM result from the bit-wise analog outputs. Further, we apply a correction to recover the signed synaptic values. Since physical conductance is non-negative (mapped to $\{0, 1\}$), while logical weights are binary signed values ($\{-1, 1\}$), the raw accumulated output must be transformed. The final synaptic result \vec{R} is computed as:

$$\vec{R} = \gamma \cdot \left(2 \cdot \vec{R}_{\text{CIM}} - \sum a_i \right) \quad (14)$$

where \vec{R}_{CIM} is the raw output from the crossbar accumulation, $\sum a_i$ is the sum of input activations (used to bias the result), and γ is a trainable scaling parameter. This step ensures the hardware output mathematically matches the intended neural network operation. More details about the algorithm-to-physical weight mapping and the physical-to-algorithm result reconstruction are in Appendix A.

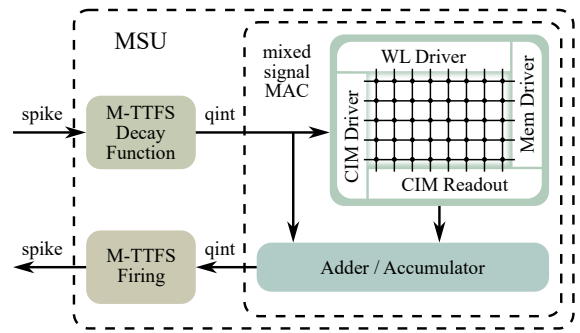


Figure 4. Memristive Synapse Unit (MSU) architecture.

3.4. Energy analysis

To evaluate the energy consumption of the SNN, we employ a hybrid modeling approach. We measure the digital energy based on a commercial 22 nm process (adopting the same spatial dataflow architecture described in Section 2.3) and calculate the analog in-memory computing energy using a physical crossbar macro (Ye et al., 2023). Consequently, the total energy for fully connected layer E_{FC} is divided into two components:

$$E_{\text{FC}} = E^{\text{analog}} + E^{\text{digital}} \quad (15)$$

The digital component, E^{digital} , accounts for spike data movement, spike generation, and static leakage (which occurs regardless of spiking activity):

$$E_{\text{digital}} = BSC_o \left[\underbrace{C_i T (s_r E^{\text{move}})}_{\text{spike movement}} + E_{\text{leak}} \right. \\ \left. + \underbrace{T \cdot (E_{\text{CMP}} + E_{\text{th}}^{\text{Read}})}_{\text{thresholding}} \right] \quad (16)$$

The analog component, E^{analog} , covers the mixed-signal multiply-accumulate (MAC) operations and the digital mapping overhead required for analog computing:

$$E_{\text{analog}} = BS \left[\underbrace{T \cdot C_i \cdot E_{\text{sum}}}_{\text{input vector element sum}} \right. \\ \left. + C_o \cdot \left(\underbrace{\log T \cdot (C_i \cdot E_{\text{MAC}}^{\text{avg}})}_{\text{analog computing}} + \underbrace{E_{\text{ACC}}}_{\text{shift\&add}} + \underbrace{E_{\text{map}}}_{\text{Analog mapping}} \right) \right] \quad (17)$$

The analog in-memory computing energy is determined by the quantization bit count $\log T$, the total number of MAC operations ($N_o^{\text{fc}} C_i$), and the average energy per 1-bit MAC in the crossbar. The digital accumulation energy consists of the input summation energy E_{sum} over T input cycles, the shift-and-add energy E_{add} (denoted as E_{ACC} in the equation) across $\log T$ computing cycles, and the one-time mapping energy E_{map} using in Equation 14.

For the attention score calculation, we employ a time-based accumulation (ACC) strategy. Instead of executing decay and MAC operations for every incoming spike (as in Equation 18), we first accumulate the synaptic inputs and subsequently multiply the aggregated membrane potential by the scaling decay function at each time step. The specific architecture and implementation details are provided in the Appendix B.

$$E_{\text{qkv}} = N_o^{\text{qkv}} \cdot \left[d_k T \left(s_r \underbrace{(E_{\text{ACC}} + E_{\text{move}}^{\text{sparse}} + E_{\text{KV}}^{\text{Read}})}_{\text{Spike Processing}} \right) + E_{\text{leak}} \right. \\ \left. + \underbrace{T(E_{\text{encoding}} + E_{\text{MAC}})}_{\text{Scaling at each time step}} + \underbrace{T(E_{\text{CMP}} + E_{\text{th}}^{\text{Read}})}_{\text{Thresholding}} \right] \quad (18)$$

4. Results

In this section, we evaluate Matterhorn on seven GLUE benchmark tasks and compare its performance against both quantized ANN baselines and state-of-the-art SNN models. We then analyze the energy efficiency of our design, followed by an ablation study on the proposed M-TTFS encoding scheme. All experiments use BERT_{base} as the teacher for knowledge distillation with a 4-bit simulation window corresponding to $T = 16$ time steps. To quantify energy consumption, we synthesized verilog implementations of key components on a commercial 22 nm process, measuring unit costs for operations, and per-bit energy for inter-core spike movement and SRAM access. Details are provided in the Appendix G.

4.1. GLUE Benchmark Performance

As detailed in Table 1, our proposed M-TTFS-based Matterhorn establishes a state-of-the-art accuracy among spiking transformers, both with and without the dead zone constraint ($k = 1$ and $k = 0$). When compared to existing 1-bit baselines with comparable parameter counts, Matterhorn consistently outperforms the previous leading method, Spiking Otters (Yan et al., 2025a). Specifically, with a dead zone radius of $k = 0$, it achieves an average accuracy of 85.87% (a 2.65% improvement), and maintains a 1.42% lead even under the stricter sparsity constraint of $k = 1$ (84.64%). On the challenging RTE task, Matterhorn ($k = 0$) reaches 72.56%, exceeding Spiking Otters by over 3.6% and approaching the performance of the full-precision BERT baseline. Furthermore, despite its reduced size, Matterhorn ($k = 0$) surpasses larger spiking baselines, outperforming the 50M-parameter SpikingBERT (80.83%) by 5.04%.

4.2. M-TTFS Ablation study

To evaluate the proposed encoding scheme, we analyze the impact of both M-TTFS encoding and the dead-zone radius k on spike time distribution, energy consumption, and model accuracy. Figure 5 illustrates the spike time distributions on the SST-2 dataset. As shown in Figure 5(a), the standard TTFS baseline exhibits a dense firing pattern with only 0.26% silent neurons, resulting in high spike movement energy cost. In contrast, M-TTFS significantly shifts this

Table 1. Performance comparison on the GLUE benchmark. All scores represent accuracy except for STS B which uses Pearson correlation. The asterisk symbol indicates that the model size was not reported in the original paper. Bold text highlights the best performance among SNN models, while an underbar denotes the second-best result.

Model	Size	QQP	MNLI-m	SST-2	QNLI	RTE	MRPC	STS-B	Average
BERT _{base} (Devlin et al., 2019)	418M	91.3	84.7	93.3	91.7	72.6	88.2	89.4	87.31
DistilBERT (Sanh et al., 2019)	207M	88.5	82.2	91.3	89.2	59.9	87.5	86.9	83.64
TinyBERT ₆ (Jiao et al., 2020)	207M	-	84.6	93.1	90.4	70.0	87.3	83.7	84.85
Q2BERT (Zhang et al., 2020)	43.0M	67.0	47.2	80.6	61.3	52.7	68.4	4.4	54.51
BiT (Liu et al., 2022)	13.4M	82.9	77.1	87.7	85.7	58.8	79.7	71.1	77.57
SpikingFormer (Zhou et al., 2023)	*	83.8	67.8	82.7	74.6	58.8	74.0	72.3	73.43
SpikingBERT (Bal & Sengupta, 2024)	50M	86.8	78.1	88.2	85.2	66.1	79.2	82.2	80.83
SpikeLM (Xing et al., 2024b)	*	87.9	76.0	86.5	84.9	65.3	78.7	84.3	80.51
1-bit SpikeLM (Xing et al., 2024b)	*	87.2	74.9	86.6	84.5	65.7	78.9	83.9	80.24
1-bit Spiking Sorbet (Tang et al., 2025)	13.4M	86.5	77.3	90.4	86.1	60.3	79.9	78.1	79.80
1-bit Spiking Otters (Yan et al., 2025a)	13.4M	87.67	78.50	91.28	86.42	68.95	84.56	85.19	83.22
1-bit Matterhorn(k=0)	13.4M	89.55	81.81	92.55	89.55	72.56	88.24	86.82	85.87
1-bit Matterhorn(k=1)	13.4M	<u>88.32</u>	80.70	<u>91.63</u>	87.74	71.84	<u>86.27</u>	86.00	84.64

distribution by remapping the most frequent spike time to the zero-energy state. In our setup ($T = 16$), I_{\max} is fixed at 7 globally across all symmetric quantized layers and heads. With $k = 0$ (Figure 5(b)), the silence rate rises to 34.0%. Expanding the dead zone to $k = 1$ and $k = 2$ (Figures 5(c-d)) further increases sparsity to 61.2% and 76.4% respectively.

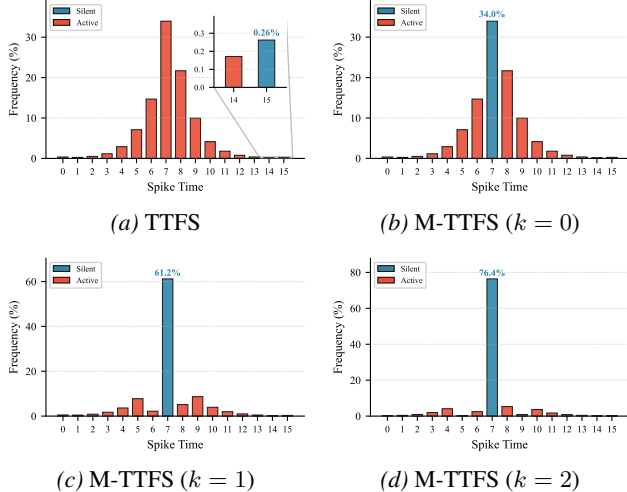


Figure 5. Comparison of spike time distributions on the SST-2 dataset. We compare the traditional TTFS baseline (a) with our proposed M-TTFS method under different dead-zone parameters.

Figure 6 quantifies the trade-off between spike movement energy and accuracy on the SST-2 dataset. Compared to the standard TTFS baseline, M-TTFS with $k=0$ reduces energy consumption to 4.75 mJ while maintaining an identical accuracy of 92.55%. Subsequently, increasing the dead zone to $k = 1$ yields the optimal balance point, decreasing energy use by 59% to 2.84 mJ with a negligible accuracy drop of only 0.9%. Finally, for $k \geq 2$, the model enters a regime of aggressive sparsity where energy drops further to 1.80 mJ,

but accuracy begins to degrade noticeably to 88.42%, suggesting that $k = 1$ offers the most favorable configuration for resource-constrained deployment. A full ablation study is provided in the Appendix F.

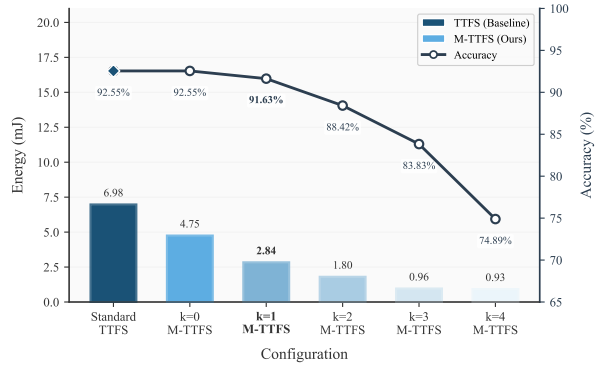


Figure 6. Energy-Accuracy Trade-off Analysis.

4.3. Energy Ablation Study

We show the energy benefits of the proposed Matterhorn in Table 2. Starting from a 16.80 mJ baseline, M-TTFS lowers consumption to 12.24 mJ by minimizing spike traffic. The dead zone ($k = 1$) further reduces this to 8.31 mJ, cutting digital computation by around 60%. Finally, by integrating our MSU, we achieve an optimal energy consumption of 6.14 mJ, representing a 2.7 \times total reduction.

4.4. Energy comparison with SOTA spiking transformer

Figure 7 benchmarked the energy efficiency of Matterhorn against leading spiking transformers. Our model demonstrates superior efficiency across all comparisons. Even without hardware acceleration, Matterhorn ($k = 1$) reduces energy consumption to 8.31 mJ, marking a 42% improvement over the previous most efficient method,

Table 2. Energy consumption (mJ) comparison per transformer block on SST-2 dataset.

Method	Spike mov.	Weight acc.	Leakage	Computing			Total
				Digital	Analog	Total	
Traditional TTFS	6.98	4.65	1.91	3.27	0	16.80	
+ M-TTFS	4.75	3.33	1.91	2.25	0	12.24	
+ dead zone (k=1)	2.84	2.20	1.91	1.37	0	8.31	
+ MSU	2.84	0.69	1.91 ^a	0.20	0.50 ^b	6.14	

^a An upper bound, assuming not removing digital modules introduced in previous designs.

^b The analog energy includes both active computation and static leakage.

Spiking Otters (14.21 mJ). When deployed with our specialized MSU, energy consumption further decreases to 6.14 mJ, achieving a total 57% reduction compared to Otters. The advantage is even more pronounced against larger-scale baselines: Matterhorn is approximately 4.24× more efficient than SpikingLM, 6.98× more efficient than Sorbet, and over 13.13× more efficient than SpikingBERT.

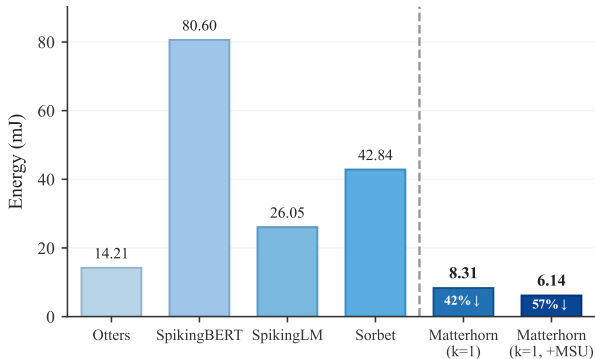


Figure 7. Comparison with SOTA spiking transformer

We further compare Matterhorn ($k = 1$) with MSU against its equivalent QNN baseline, as derived in Proposition 1. While both models achieve identical accuracy due to their mathematical equivalence, Matterhorn demonstrates superior efficiency. For the same transformer block on SST-2 dataset, the QNN consumes 14.47 mJ, whereas Matterhorn delivers a 2.35× improvement in energy efficiency.

5. Discussion

Robustness to Analog Noise We exclude explicit noise modeling because the hardware design of the MSU inherently suppresses analog non-idealities. Unlike multi-level cell approaches that suffer from tight sensing margins, our architecture utilizes single-bit (binary) weights. This maximizes the read margin and ensures high conductance uniformity. Furthermore, the underlying CIM circuit (Ye et al., 2023) mitigates process variation, leakage, and parasitic effects at the hardware level. By performing integration in a bit-serial manner (1bx1b VMM), we avoid the non-linear error accumulation typical of multi-bit analog computing. Consequently, hardware noise remains negligible and does

not degrade the accuracy of the proposed model.

Hardware Area Efficiency The mixed-signal MSU achieves high area efficiency by leveraging high-density analog CIM and optimizing digital layout. The primary area cost stems from the analog CIM array. Based on the 2T1R cell density of about $0.59 \mu\text{m}^2/\text{bit}$ (Ye et al., 2023), a 256×256 (64Kb) macro occupies approximately 0.072 mm^2 , which is comparable to novel ASIC accelerators (Zhu et al., 2025). To minimize footprint, we synthesize the digital logic within the unused silicon area at the macro corners (shown in Appendix C). For large-scale models, we employ a tiled architecture where multiple macros compute partial results that are aggregated digitally. A single transformer block requires 108 macros. Additionally, our M-TTFS encoding reduces interconnect complexity. By transmitting information via 1-bit spikes rather than multi-bit integers, we alleviate routing congestion and lower the total wire count. Even after accounting for routing overhead, the total silicon area for a complete transformer block remains under 10 mm^2 , demonstrating the physical scalability of our approach. The entire model fits within a 120 mm^2 footprint, a size comparable to modern commercial CPUs (Munger et al., 2023) and GPUs (Keller et al., 2023)

6. Conclusion

In this paper, we introduced Matterhorn, a high-performance spiking transformer designed to overcome the energy inefficiency caused by data movement in SNNs. We propose masked time-to-first-spike (M-TTFS), which remaps the most frequent spike time to the silent state. We further extend it with a dead zone to further increase the silence and reduce spike movement. We also introduce a memristive synapse unit (MSU) based on compute-in-memory that keeps weights in place and performs analog integration in memory to cut weight access cost. On the GLUE benchmark, Matterhorn ($k = 1$) achieves an average score of 84.64%, surpassing state-of-the-art Spiking Transformers by 1.42%, while simultaneously reducing energy consumption to 6.14 mJ (with MSU). The entire Spiking Transformer fits within a 120 mm^2 footprint, showing the physical viability of deploying Matterhorn on chips.

7. Impact Statement

This paper presents work whose goal is to advance the field of Machine Learning. There are many potential societal consequences of our work, none of which we feel must be specifically highlighted here.

References

Bae, J., Won, J., and Shim, W. The rise of memtransistors for neuromorphic hardware and in-memory computing. *Nano Energy*, 126:109646, 2024. doi: <https://doi.org/10.1016/j.nanoen.2024.109646>.

Bal, M. and Sengupta, A. Spikingbert: Distilling bert to train spiking language models using implicit differentiation. In *Proceedings of the AAAI conference on artificial intelligence*, volume 38, pp. 10998–11006, 2024.

Che, K., Fang, W., Ma, Z., Huang, Y., Xue, P., Yuan, L., Masquelier, T., and Tian, Y. Efficiently training time-to-first-spike spiking neural networks from scratch, 2025. URL <https://arxiv.org/abs/2410.23619>.

Dampfhofer, M., Mesquida, T., Valentian, A., and Anghel, L. Are snns really more energy-efficient than anns? an in-depth hardware-aware study. *IEEE Transactions on Emerging Topics in Computational Intelligence*, 7(3):731–741, 2023. doi: 10.1109/TETCI.2022.3214509.

Davies, M., Srinivasa, N., Lin, T.-H., Chinya, G., Cao, Y., Choday, S. H., Dimou, G., Joshi, P., Imam, N., Jain, S., Liao, Y., Lin, C.-K., Lines, A., Liu, R., Mathaikutty, D., McCoy, S., Paul, A., Tse, J., Venkataraman, G., Weng, Y.-H., Wild, A., Yang, Y., and Wang, H. Loihi: A neuromorphic manycore processor with on-chip learning. *IEEE Micro*, 38(1):82–99, 2018. doi: 10.1109/MM.2018.112130359.

Devlin, J., Chang, M.-W., Lee, K., and Toutanova, K. Bert: Pre-training of deep bidirectional transformers for language understanding. In *Proceedings of the 2019 conference of the North American chapter of the association for computational linguistics: human language technologies, volume 1 (long and short papers)*, pp. 4171–4186, 2019.

Jiao, X., Yin, Y., Shang, L., Jiang, X., Chen, X., Li, L., Wang, F., and Liu, Q. Tinybert: Distilling bert for natural language understanding. In *Findings of the Association for Computational Linguistics: EMNLP 2020*, pp. 4163–4174, 2020.

Keller, B., Venkatesan, R., Dai, S., Tell, S. G., Zimmer, B., Sakr, C., Dally, W. J., Gray, C. T., and Khailany, B. A 95.6-ops/w deep learning inference accelerator with per-vector scaled 4-bit quantization in 5 nm. *IEEE Journal of Solid-State Circuits*, 58(4):1129–1141, April 2023. doi: 10.1109/JSSC.2023.3234893.

Khan, A. A., Farzaneh, H., Friebel, K. F. A., Fournier, C., Chelini, L., and Castrillon, J. Cinn (cinnamon): A compilation infrastructure for heterogeneous compute in-memory and compute near-memory paradigms. In *Proceedings of the 29th ACM International Conference on Architectural Support for Programming Languages and Operating Systems, Volume 4*, pp. 31–46, 2024.

Liu, Z., Oguz, B., Pappu, A., Xiao, L., Yih, S., Li, M., Krishnamoorthi, R., and Mehdad, Y. Bit: Robustly binarized multi-distilled transformer. *Advances in neural information processing systems*, 35:14303–14316, 2022.

Munger, B., Wilcox, K., Sniderman, J., Tung, C., Johnson, B., Schreiber, R., Henrion, C., Gillespie, K., Burd, T., Fair, H., Johnson, D., White, J., McLelland, S., Bakke, S., Olson, J., McCracken, R., Pickett, M., Horuchi, A., Nguyen, H., and Jackson, T. H. “zen 4”: The amd 5nm 5.7ghz x86-64 microprocessor core. In *2023 IEEE International Solid-State Circuits Conference (ISSCC)*, pp. 38–39, Feb 2023. doi: 10.1109/ISSCC42615.2023.10067540.

Prabhakar, R., Jairath, S., and Shin, J. L. Samanova sn10 rdu: A 7nm dataflow architecture to accelerate software 2.0. In *2022 IEEE International Solid-State Circuits Conference (ISSCC)*, volume 65, pp. 350–352. IEEE, 2022.

Sanh, V., Debut, L., Chaumond, J., and Wolf, T. Distilbert, a distilled version of bert: smaller, faster, cheaper and lighter. *arXiv preprint arXiv:1910.01108*, 2019.

Tang, K., Yan, Z., and Wong, W.-F. Sorbet: A neuromorphic hardware-compatible transformer-based spiking language model. In *Forty-second International Conference on Machine Learning*, 2025.

Wang, C., Yan, Z., Zhou, Z., Chen, X., and Wong, W.-F. Energy-efficient and dequantization-free Q-LLMs: A spiking neural network approach to salient value mitigation. *arXiv preprint arXiv:2510.19498*, 2025.

Wei, W., Zhang, M., Qu, H., Belatreche, A., Zhang, J., and Chen, H. Temporal-coded spiking neural networks with dynamic firing threshold: Learning with event-driven backpropagation. In *Proceedings of the IEEE/CVF international conference on computer vision*, pp. 10552–10562, 2023.

Wen, T.-H., Hsu, H.-H., Khwa, W.-S., Huang, W.-H., Ke, Z.-E., Chin, Y.-H., Wen, H.-J., Chang, Y.-C., Hsu, W.-T., Lo, C.-C., Liu, R.-S., Hsieh, C.-C., Tang, K.-T., Teng, S.-H., Chou, C.-C., Chih, Y.-D., Chang, T.-Y. J., and Chang, M.-F. 34.8 a 22nm 16mb floating-point ReRAM compute-in-memory macro with 31.2tflops/w for AI edge devices. In *2024 IEEE International Solid-State Circuits Conference (ISSCC)*, volume 67, pp. 580–582, Feb 2024. doi: 10.1109/ISSCC49657.2024.10454468.

Xiao, G., Lin, J., Seznec, M., Wu, H., Demouth, J., and Han, S. Smoothquant: Accurate and efficient post-training quantization for large language models. In *International conference on machine learning*, pp. 38087–38099. PMLR, 2023.

Xing, X., Gao, B., Zhang, Z., Clifton, D. A., Xiao, S., Du, L., Li, G., and Zhang, J. Spikelm: Scaling up spiking neural network to large language models via saliency-based spiking. *arXiv preprint arXiv:2407.04752*, 2024a.

Xing, X., Zhang, Z., Ni, Z., Xiao, S., Ju, Y., Fan, S., Wang, Y., Zhang, J., and Li, G. Spikelm: Towards general spike-driven language modeling via elastic bi-spiking mechanisms. In *Forty-first International Conference on Machine Learning*, 2024b.

Yan, Z., Zhou, J., and Wong, W.-F. CQ⁺ training: Minimizing accuracy loss in conversion from convolutional neural networks to spiking neural networks. *IEEE Transactions on Pattern Analysis and Machine Intelligence*, 45(10):11600–11611, 2023. doi: 10.1109/TPAMI.2023.3286121.

Yan, Z., Bai, Z., and Wong, W.-F. Reconsidering the energy efficiency of spiking neural networks. *arXiv preprint arXiv:2409.08290*, 2024.

Yan, Z., Mao, J., Liu, Q., Li, F., Pan, G., Luo, T., Zhu, B., and Wong, W.-F. Otters: An energy-efficient spikingtransformer via optical time-to-first-spike encoding. *arXiv preprint arXiv:2509.18968*, 2025a.

Yan, Z., Tang, K., Zhou, J., and Wong, W.-F. Low latency conversion of artificial neural network models to rate-encoded spiking neural networks. *IEEE Transactions on Neural Networks and Learning Systems*, pp. 1–12, 2025b. doi: 10.1109/TNNLS.2025.3526374.

Ye, W., Wang, L., Zhou, Z., An, J., Li, W., Gao, H., Li, Z., Yue, J., Hu, H., Xu, X., Yang, J., Liu, J., Shang, D., Zhang, F., Tian, J., Dou, C., Liu, Q., and Liu, M. A 28-nm RRAM computing-in-memory macro using weighted hybrid 2t1r cell array and reference subtracting sense amplifier for ai edge inference. *IEEE Journal of Solid-State Circuits*, 58(10):2839–2850, Oct 2023. doi: 10.1109/JSSC.2023.3280357.

Zhang, W., Hou, L., Yin, Y., Shang, L., Chen, X., Jiang, X., and Liu, Q. Ternarybert: Distillation-aware ultra-low bit bert. In *Proceedings of the 2020 Conference on Empirical Methods in Natural Language Processing (EMNLP)*, pp. 509–521, 2020.

Zhao, L., Huang, Z., Ding, J., and Yu, Z. TTFSFormer: A TTFS-based lossless conversion of spiking transformer. In *Forty-second International Conference on Machine Learning*, 2025.

Zhou, C., Yu, L., Zhou, Z., Ma, Z., Zhang, H., Zhou, H., and Tian, Y. Spikingformer: Spike-driven residual learning for transformer-based spiking neural network. *arXiv preprint arXiv:2304.11954*, 2023.

Zhu, Z., Zhou, X., Wang, C., Tian, L., Huang, Z., and Zhu, Y. Bit-sparsity aware acceleration with compact CSD code on generic matrix multiplication. *IEEE Transactions on Computers*, 74(2):414–426, Feb 2025. doi: 10.1109/TC.2024.3483632.

A. Analog-Centric Mixed-Signal In-Memory Computing

Analog-centric in-memory computing leverages device physics to perform matrix multiplication directly within memory arrays, eliminating the latency and energy costs of data movement. The core mechanism maps multiply-accumulate (MAC) operations to circuit current dynamics using two fundamental laws. First, the memory cell conductance G represents the weight W , and the applied voltage V represents the input x . By Ohm's Law, the current through a single cell is $I = V \cdot G$, physically realizing a scalar multiplication. Second, by Kirchhoff's Current Law (KCL), currents from parallel branches sum automatically at a common node. This allows the total current $I_{total} = \sum(V_i \cdot G_i)$ to physically represent the vector dot product $\vec{y} = \vec{x} \cdot \mathbf{W}$ directly on the interconnect wire.

To implement this at scale, we utilize a crossbar array composed of nT1R (n-Transistor, 1-Resistor) cells, as shown in Figure 8. Each cell contains a resistive memory device, which stores the weight as conductance, and an access transistor that acts as a selector switch. The array utilizes three sets of orthogonal lines for control and data: Word Lines (WL) control the transistor gates to select active rows; Source Lines (SL) supply the analog input voltages; and Bit Lines (BL) collect the accumulated summation current for each column (Figure 9). Ideally, when a row is activated, the resulting column currents are read by Analog-to-Digital Converters (ADCs), which discretize the analog values into digital indices for subsequent processing.

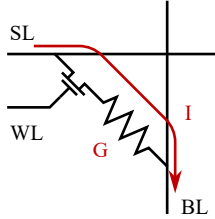


Figure 8. Typical structure of the nT1R cell. The resistive device stores weights via conductance, while the transistor gates control access.

Take a 4-column-3-row array with 1-bit activation and 1-bit weight for example. Let the SLs share a supply voltage $V = 0.1$ Volt, the inputs control corresponding WLs to turn on or turn off a whole row, and the values stored in the 1-bit devices are conductance $G_1 = 100\mu$ Siemens for logic 1 and $G_0 = 1\mu$ Siemens for logic 0. The current at each BL is the summation of all cells from the same column. The BL current values, 10.1μ Ampere, 0.2μ Ampere, 10.1μ Ampere, and 20.0μ Ampere, are sampled by ADCs as digital indexes 1, 0, 1, 2, respectively.

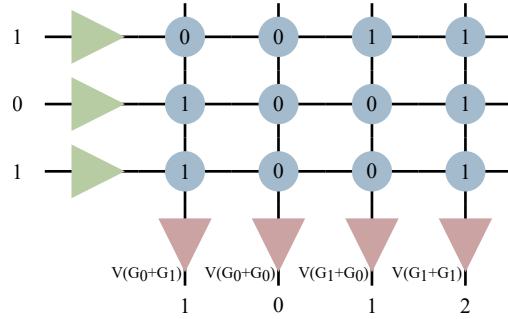


Figure 9. Schematic of the typical analog crossbar architecture. Inputs are applied to Source Lines, and accumulated currents are read from Bit Lines.

Since analog computation is most efficient at lower precision, we employ a mixed-signal strategy that processes inputs in a bit-serial manner. We decompose a n -bit activation vector \vec{A} into binary bit-vectors \vec{A}_n . The full vector-matrix multiplication (VMM) is then reconstructed as a weighted sum of partial binary products:

$$\vec{R} = \vec{A} \times \mathbf{W} = \sum_n (\vec{A}_n \times \mathbf{W}) 2^n = \sum_n \vec{R}_n 2^n, \quad \vec{R}_n = \vec{A}_n \times \mathbf{W} \quad (19)$$

In this scheme, the analog crossbar computes the core binary VMM $\vec{R}_n = \vec{A}_n \times \mathbf{W}$ in a single step, and a digital accumulator synthesizes the final result \vec{R} using shift-and-add operations. This hybrid approach combines the energy efficiency of analog computing with the precision-flexibility of digital logic.

A critical challenge in this architecture is mapping signed algorithm weights to physical conductance, which is strictly non-negative. To address this, we employ a bias-and-scale strategy. Algorithmic binary weights $\{-1, 1\}$ are mapped to physical conductance states $\{0, 1\}$, represented mathematically as $\mathbf{W}_{\text{CIM}} = (\mathbf{W} + 1)/2$. Consequently, the raw output from the crossbar is a shifted version of the desired result. To recover the correct signed synaptic value \vec{R} , we apply a linear correction in the digital domain:

$$\vec{R} = \vec{A} \times \mathbf{W} = 2 \cdot \vec{A} \times \mathbf{W}_{\text{CIM}} - \sum a_i = 2 \cdot \vec{R}_{\text{CIM}} - \sum a_i \quad (20)$$

where \vec{R}_{CIM} is the raw accumulated output from the crossbar and $\sum a_i$ accounts for the input-dependent bias introduced by the weight mapping.

B. Time-Based Accumulation for Self-Attention

The scaled dot product operation processing QKV matrices for self-attention does not require stationary weight matrices. An efficient way for this operation is the time-based accumulation strategy, which calculates the corresponding vector-matrix multiplication at the time when spikes arrive.

B.1. Time-based accumulation

The spike train is transferred one bit each cycle, where time carries the spike value information. The time-based accumulation replaces the MAC operation using time-serial accumulation. For the t -th cycle receiving a group of spike trains, all weights corresponding to the spikes (w_i for $s_i = 1$) are summed up, then multiplied by the time decay value $f(t)$, producing a partial result V_t :

$$V_t = f(t) \cdot \sum_i w_i |_{s_i=1} + V_{t-1} \quad (21)$$

B.2. Attention using time-based accumulation

Matrix multiplications in the self-attention operations are handled using time-based accumulation blocks. The input Q matrix is a group of spike trains, and the KV matrices are as integers. The first is to calculate $Q \times K^T$ and apply the Softmax function. The intermediate results are transferred as spike trains. Consequently, intermediate results are multiplied by the V matrix to produce the self-attention score. Multiple time-based accumulation blocks work in parallel to handle the long tokens. Each block produces a partial value for the output vector element, and the partial values are summed up in the last block to obtain the output result.

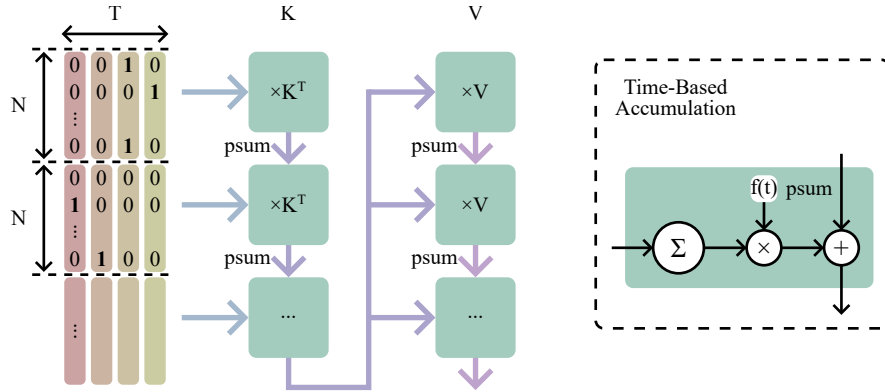


Figure 10. Self attention operation using time-based accumulation.

C. Floorplan of the Mixed-Signal MSU

Prior work (Ye et al., 2023) demonstrated an 8Kb (64×128) array prototype with a cell size of about $0.585 \mu\text{m}^2$. As a research test chip, the original layout allocated significant area to peripheral test circuits, resulting in low array efficiency.

For application-level estimation, we project metrics based on a standard 256×256 (64Kb) crossbar configuration, optimizing the peripheral layout for production density.

Figure 11 illustrates the proposed floorplan for the MSU. Analog crossbar arrays typically result in unutilized silicon area at the macro corners. We leverage this space to embed necessary digital components, including decoders, adders, and accumulators. To ensure signal integrity, we allocate a 6 μm keep-out zone between the analog and digital domains, isolating sensitive analog signals from digital switching noise (e.g., ground bounce). Under these constraints, the total area for a complete 256×256 binary VMM macro is estimated at 0.072 mm².

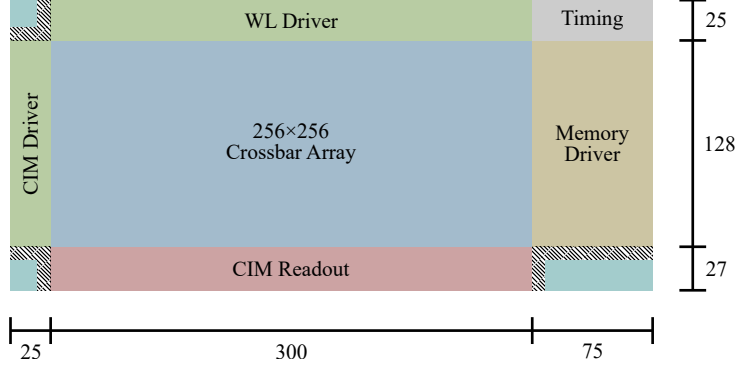


Figure 11. Schematic floorplan of the MSU. Digital logic is synthesized in the corner regions of the analog macro. A guard ring (keep-out zone) isolates the analog array from digital interference. All dimensions are in μm .

D. Proof for Proposition 1

D.1. Integration Phase Equivalence

We show that during integration, the accumulated membrane potential V_j^l of the SNN neuron equals the QNN pre-activation a_j^l , i.e., $V_j^l = a_j^l$, under Proposition 1.

Let the quantized output from layer $l-1$ in the QNN be

$$x_{q,i}^{l-1} = \alpha^{l-1} q_i^{l-1}, \quad (22)$$

where $q_i^{l-1} \in \mathbb{Z}$ is obtained with resolution T . By Proposition 1(1), $T = 2^n$, hence $T/2 \in \mathbb{Z}$. Proposition 1(2) aligns the most frequent integer activation μ with I_{\max} via

$$\mu = \frac{T}{2} - 1 - I_{\max}, \quad (23)$$

and collapses a k -bounded neighborhood to μ :

$$q_i^{l-1} \leftarrow \mu \quad \text{if} \quad |q_i^{l-1} - \mu| \leq k. \quad (24)$$

We encode each integer q_i^{l-1} using M-TTFS with at most one spike at time

$$t_i = \frac{T}{2} - q_i^{l-1} - 1. \quad (25)$$

Thus larger q_i^{l-1} yields an earlier spike, and in particular $q = \mu$ maps to $t_i = I_{\max}$, matching Proposition 1(2).

Proposition 1(3) defines the flattened M-TTFS amplitude

$$f(t) = \begin{cases} \mu & \text{if } |t - I_{\max}| \leq k, \\ \frac{T}{2} - 1 - |t| & \text{otherwise.} \end{cases} \quad (26)$$

Evaluating at t_i gives $f(t_i) = q_i^{l-1}$ in all cases. Indeed, if $|t_i - I_{\max}| \leq k$, then by (24) we have $q_i^{l-1} = \mu$ and $f(t_i) = \mu = q_i^{l-1}$. Otherwise, since $t_i \in \mathbb{Z}$ (because $T/2$ and q_i^{l-1} are integers), $\lfloor t_i \rfloor = t_i$, and

$$f(t_i) = \frac{T}{2} - 1 - t_i = \frac{T}{2} - 1 - \left(\frac{T}{2} - q_i^{l-1} - 1 \right) = q_i^{l-1}. \quad (27)$$

For a presynaptic spike from neuron i at time t_i , the *Matterhorn* PSP contribution to neuron j is

$$\epsilon(w_{ij}^l, t_i) = w_{ij}^l \cdot \alpha^{l-1} \cdot f(t_i). \quad (28)$$

Using (27) and $x_{q,i}^{l-1} = \alpha^{l-1} q_i^{l-1}$, we obtain

$$\epsilon(w_{ij}^l, t_i) = w_{ij}^l \cdot \alpha^{l-1} \cdot q_i^{l-1} = w_{ij}^l x_{q,i}^{l-1}. \quad (29)$$

The integrated membrane potential at layer l sums all incoming PSPs and adds the bias:

$$V_j^l = \sum_i \epsilon(w_{ij}^l, t_i) + b_j^l = \sum_i w_{ij}^l x_{q,i}^{l-1} + b_j^l. \quad (30)$$

By the definition of the QNN pre-activation,

$$a_j^l = \sum_i w_{ij}^l x_{q,i}^{l-1} + b_j^l, \quad (31)$$

we conclude $V_j^l = a_j^l$, proving the integration-phase equivalence.

D.2. Firing Phase Equivalence

We next show that the QNN masking operation matches the SNN dead zone, and that the SNN firing time t_j^l precisely encodes the (masked) quantized output $x_{q,j}^l$.

From the integration result, we have $V_j^l = a_j^l$. The SNN neuron fires at the earliest time $t \in [0, T - 1]$ such that its membrane potential reaches the time-varying threshold in Proposition 1(4):

$$a_j^l \geq \theta^l(t) = \alpha^l \left(\frac{T}{2} - 1 - \lfloor t \rfloor \right). \quad (32)$$

Let $A = \frac{T}{2} - 1 \in \mathbb{Z}$ and $r = \frac{a_j^l}{\alpha^l}$. Since $\alpha^l > 0$, (32) is equivalent to

$$r \geq A - \lfloor t \rfloor \iff \lfloor t \rfloor \geq A - r. \quad (33)$$

Because A is an integer, the earliest time satisfying the inequality is obtained by choosing

$$t_j^l = \text{Clip}(\lceil A - r \rceil, 0, T - 1), \quad (34)$$

which implements the saturation induced by the finite simulation window.

Define the integer value decoded from the firing time (i.e., the value a spike at time t represents outside the dead zone) as

$$\hat{q}_j^l = A - t_j^l. \quad (35)$$

Ignoring only the boundary clipping in (34) for the moment, we use the identity $A - \lceil A - r \rceil = \lfloor r \rfloor$ (valid for integer A) to obtain

$$\hat{q}_j^l = A - \left\lceil A - \frac{a_j^l}{\alpha^l} \right\rceil = \left\lfloor \frac{a_j^l}{\alpha^l} \right\rfloor. \quad (36)$$

With (34), the finite window simply clips \hat{q}_j^l into the representable range $[-\frac{T}{2}, \frac{T}{2} - 1]$:

$$\hat{q}_j^l = \text{Clip}\left(\left\lfloor \frac{a_j^l}{\alpha^l} \right\rfloor, -\frac{T}{2}, \frac{T}{2} - 1\right) = \text{Clip}\left(\left\lfloor \frac{a_j^l}{\alpha^l} \right\rfloor, -2^{n-1}, 2^{n-1} - 1\right) \quad (37)$$

Therefore, \hat{q}_j^l matches the *unmasked* QNN integer quantization result q_j^l .

We now connect the QNN mask to the SNN dead zone. Proposition 1(2) defines the masked QNN integer output as

$$\bar{q}_j^l = \begin{cases} \mu, & \text{if } |\hat{q}_j^l - \mu| \leq k, \\ \hat{q}_j^l, & \text{otherwise,} \end{cases} \quad (38)$$

where $\mu = A - I_{\max}$ aligns the most frequent activation with I_{\max} . Proposition 1(3) defines the flattened M-TTFS decoding function

$$f(t) = \begin{cases} \mu, & \text{if } |t - I_{\max}| \leq k, \\ A - \lfloor t \rfloor, & \text{otherwise.} \end{cases} \quad (39)$$

Since t_j^l in (34) is integer, $\lfloor t_j^l \rfloor = t_j^l$. Using (35) and $\mu = A - I_{\max}$, we have

$$|t_j^l - I_{\max}| \leq k \iff |(A - \hat{q}_j^l) - (A - \mu)| \leq k \iff |\hat{q}_j^l - \mu| \leq k. \quad (40)$$

Combining (39) and (40) yields

$$f(t_j^l) = \begin{cases} \mu, & \text{if } |\hat{q}_j^l - \mu| \leq k, \\ A - t_j^l = \hat{q}_j^l, & \text{otherwise,} \end{cases} \Rightarrow f(t_j^l) = \bar{q}_j^l. \quad (41)$$

Thus, the QNN mask around μ is exactly implemented by the SNN dead zone around I_{\max} : all outputs whose integer codes lie in the k -neighborhood of μ are mapped to the same decoded value μ via firing times inside $|t - I_{\max}| \leq k$.

E. Asymmetric variant to M-TTFS

While focusing on symmetric quantization, transformers often use asymmetric activations (e.g., Softmax scores or ReLU outputs which are non-negative). We expand the proof to cover this case.

For asymmetric quantization, we compute the quantized output $x_{q,j}^l$ for neuron j as follows:

$$a_j^l = \sum_i w_{ij}^l x_{q,i}^{l-1} + b_j^l \quad (42)$$

$$q_j^l = Q(a_j^l) = \text{Clip}(\lfloor \frac{a_j^l}{\alpha^l} \rfloor, 0, 2^n - 1) \quad (43)$$

$$x_{q,j}^l = \alpha^l \cdot q_j^l \quad (44)$$

Proposition 2. *An M-TTFS SNN layer incorporating a dead zone Ω_{dead} with radius k is functionally equivalent to a trained n -bit QNN layer (as defined above), provided the following parameter configurations are applied:*

1. *T in SNN matches the QNN resolution, as $T = 2^n$.*
2. *The most frequent QNN activation q_j^l (defined as μ) is aligned with I_{\max} in SNN, and the activation q_j^l within a k -bounded neighborhood is collapsed to μ :*

$$\begin{aligned} \mu &= T - 1 - I_{\max} \\ q_j^l &= \mu \quad \text{if } |q_j^l - \mu| \leq k \end{aligned}$$

3. *The M-TTFS encoding function $f(t)$ is flattened to μ around I_{\max} :*

$$f(t) = \begin{cases} \mu & \text{if } |t - I_{\max}| \leq k \\ T - 1 - t & \text{otherwise} \end{cases}$$

4. *The firing threshold $\theta^l(t)$ follows the step-wise decreasing function:*

$$\theta^l(t) = \alpha^l \cdot (T - 1 - \lfloor t \rfloor)$$

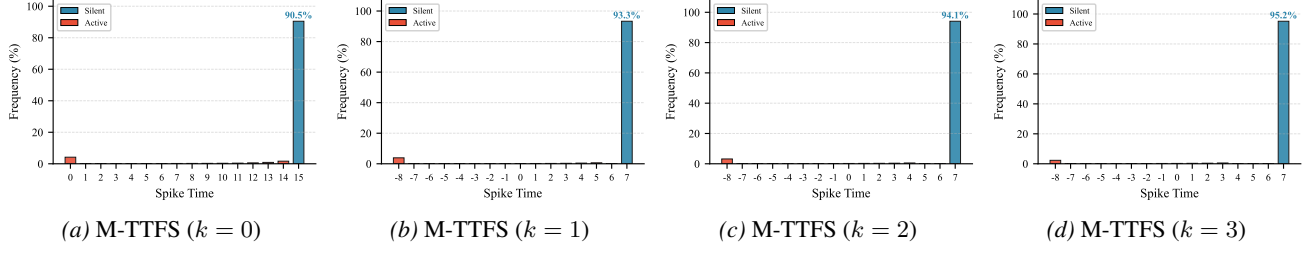


Figure 12. Comparison of spike time distributions on the SST-2 dataset for the asymmetric variant. We compare the traditional and our proposed M-TTFS method under different dead-zone parameters $k \in \{0, 1, 2, 3\}$ (a-d).

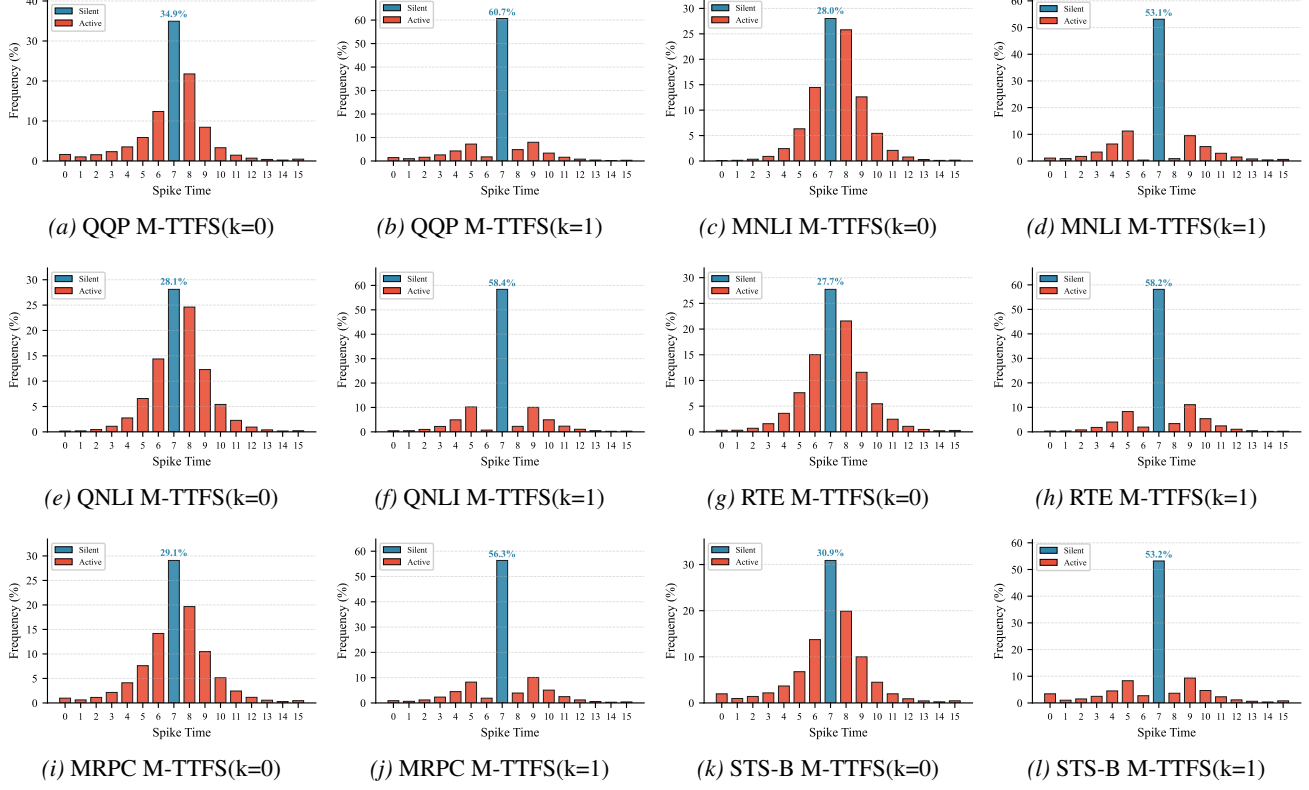


Figure 13. M-TTFS method under different dead-zone parameters $k \in \{0, 1\}$

F. Full ablation study for MTTFS for all other datasets in GLUE

We evaluate our model on seven datasets from the GLUE benchmark and report the spike time distribution of the M-TTFS method under different dead-zone parameters in Table 13.

G. Energy calculation

We evaluate energy consumption based on a standard BERT-base architecture (Batch size B=64, Sequence length S=128, Hidden dimension H=768, FFN dimension 3072, Heads h=12). All digital computation, memory access, and data movement costs are calibrated using measurements from a commercial 22nm process, while analog computing parameters are adopted from (Ye et al., 2023). For digital operations, we differentiate costs by bit-width. A standard INT4 MAC consumes 0.0848 pJ, whereas a mixed-precision MAC (1-bit input, 4-bit weight) reduces this to 0.0663 pJ. Accumulation (ACC) energy scales similarly, ranging from 0.0502 pJ (4-bit) to 0.0429 pJ (1-bit). SNN-specific neuron updates, including threshold comparison and subtraction, are modeled at 0.0502 pJ. Regarding memory and interconnects, we account for a static leakage of 0.002 pJ/cycle, a weight access cost of 0.0985 pJ/bit, and a sparse data movement cost of 0.18 pJ/bit.

Finally, the analog Compute-in-Memory (CIM) energy is modeled at 2.164 fJ/bit, which incorporates overheads for crossbar core, CIM driver, and ADC readout.

H. Energy breakdown for Matterhorn with $k = 1$ and MSU

The energy breakdown for our final spiking transformer is shown in Figure 14.

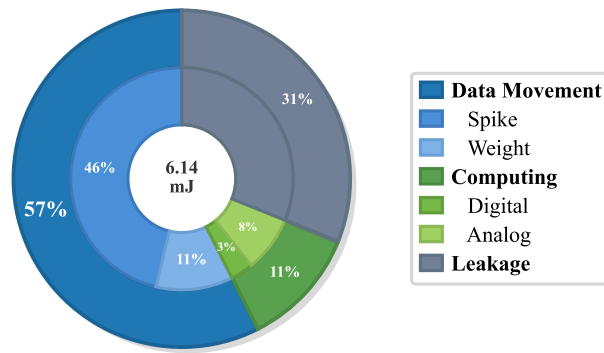


Figure 14. Matterhorn energy breakdown